AIAA 94-0820

Four-Dimensional Laser Induced Fluorescence Study of the Structure of Molecular Mixing in Turbulent Flows

Kenneth B. Southerland and Werner J.A. Dahm

Department of Aerospace Engineering
The University of Michigan
Ann Arbor, MI

32nd Aerospace Sciences Meeting & Exhibit

January 10-13, 1994 / Reno, NV

Four-Dimensional Laser Induced Fluorescence Study of the Structure of Molecular Mixing in Turbulent Flows

Kenneth B. Southerland[†] and Werner J.A. Dahm[††]

Gas Dynamics Laboratories, Department of Aerospace Engineering
The University of Michigan, Ann Arbor, MI 48109-2118

and

David R. Dowling[§]

Department of Mechanical Engineering & Applied Mechanics
The University of Michigan, Ann Arbor, MI 48109-2525

Abstract

The first experimental measurements are presented for the full three-dimensional spatial scalar energy spectrum $E_\zeta(\mathbf{k})$ resulting from the molecular mixing of a $Sc \gg 1$ conserved scalar quantity in a turbulent flow. These results are based on three- and four-dimensional laser induced fluorescence imaging measurements of a dye concentration field $\zeta(\mathbf{x},t)$ in the self-similar far-field of an axisymmetric turbulent jet at local outer-scale Reynolds numbers Re_δ between 3,000 and 6,000. Each of the resulting data sets consist of up to 3 billion individual data points, arranged into a temporal sequence of individual three-dimensional spatial data volumes, each of which consists of a series of parallel two-dimensional data planes. The resolution within each spatial data volume is finer than the local strain-limited molecular diffusion scale λ_D in all three dimensions. In addition, the temporal resolution between successive data volumes is made finer than the local diffusion scale advection time λ_D/u when time differentiation of the scalar field is of interest. This resolution, together with the signal quality achieved, permits differentiation of the data to determine the scalar gradient vector field $\nabla\zeta(\mathbf{x},t)$, and in particular the scalar dissipation rate field $(ReSc)^{-1}\nabla\zeta\cdot\nabla\zeta(\mathbf{x},t)$, throughout the data space. Results are presented for various statistics of the scalar and scalar gradient fields. The three-dimensional character of these measurements allows direct evaluation of the three-dimensional spatial scalar spectrum $E_\zeta(\mathbf{k})$ associated with turbulent mixing. The resulting isotropic spectrum function $E_\zeta(k)$, integrated from this full spectrum, is compared with its individual one-dimensional counterparts $E_\zeta(k_x)$ and $E_\zeta(k_y)$ and $E_\zeta(k_z)$ as a test of the small-scale isotropy hypothesis. These one-dimensional spatial spectra are compared with previous temporal spectrum measurements, and with Batchelor's classical theory of the high wavenumber spectrum for $Sc \gg 1$ scalar mixing in turbulent flows.

1. Introduction

The molecular mixing of one or more dynamically passive conserved scalar quantities in turbulent flows is the rate limiting step in many practical engineering problems. Among these, combustion processes in non-premixed reactant systems are especially notable. Applications range from combustor design for reacting flows in high speed airbreathing propulsion systems, to the reduction of environmental pollutants in industrial combustion systems. The arbitrary scalar quantity of interest depends on the particular problem at hand, but in general refers to any scalar property that is advected by the flow and diffuses relative to the fluid, but which is neither created nor destroyed within the flow and does not directly affect the flow field. Relevant examples include the concentration of inert tracers in a flow, the composition field in the mixing of two inert gaseous streams, or even the elemental mixture fraction in a chemically reacting turbulent flow. Often the diffusivity D of the scalar quantity being mixed is comparable to the vorticity diffusivity ν of the fluid, so the Schmidt number $Sc \equiv (\nu/D)$ is approximately unity. However, in many other cases the scalar diffusivity can be much smaller than that of the vorticity, so that $Sc \gg 1$. This occurs, for

[†] Graduate Research Assistant, Member AIAA
[††] Associate Professor, Member AIAA
[§] Assistant Professor, Member AIAA

instance, in the mixing of particulates in gaseous flows or in mixing between two or more liquid components. Moreover, recent interest in differential diffusion effects in gaseous turbulent combustion motivates an understanding of the dependence of the structure of fluid mixing on the Schmidt number. This paper focuses on the structure of $Sc \gg 1$ conserved scalar mixing in turbulent flows. We present experimental results for the statistics of the scalar and scalar gradient fields associated with mixing at the inner scales of turbulent flows. The fully three-dimensional spatial character of these measurements allows a detailed examination of the spectral structure of $Sc \gg 1$ scalar fields in turbulent mixing processes.

2. Experimental Details

The results presented here are from experiments on molecular mixing in a turbulent shear flow in water. The measurements are conducted in the self-similar far field of an axisymmetric turbulent jet issuing into an essentially quiescent medium. The conserved scalar under consideration here is the concentration of a dynamically passive dilute laser fluorescent dye (disodium fluorescein) carried by the jet fluid, for which the Schmidt number is 2075. This concentration is measured repeatedly in time at a large number of points within a small three-dimensional volume in the flow by imaging the laser induced fluorescence from dye-containing fluid onto a high-speed planar photodiode array. The flow is established by issuing jet fluid through a round nozzle into a 0.8 m $\times$ 0.8 m $\times$ 1.8 m tank filled with water, in which a very small coflow insures that there is no recirculation of dyed fluid into the imaged volume in the flow. The measurements reported here were conducted at local outer-scale Reynolds numbers $Re_\delta \equiv (u\delta/\nu)$ from 3,000 to 6,000, where u and δ are the local velocity and length scales that characterize the local mean shear in the flow. Here these are the mean centerline velocity and the local full width of the mean velocity profile. These moderate Re_δ values are dictated by the spatial and temporal resolution demanded of the measurements. However, the imaged region of the flow is quite small in comparison with the local outer scale δ, and is comparable to the local inner scale λ_ν of the flow. Each planar image from which the data are comprised typically spans less than 1/15 of the outer scale, and roughly twice the inner scale, in both directions. As a result, if these outer-scale Reynolds numbers are large enough so that on the inner scales the velocity has become independent of the outer-scale Reynolds number, then the scalar field fine structure would also be independent of Re_δ and would depend only on the Schmidt number. Furthermore, since the outer scales can influence the inner scales only through Re_δ, once the inner-scaled quantities have become independent of this outer-scale Reynolds number then all effect of the outer scales is lost. The fine structure at the inner scales seen in these measurements would then not be particular just to the turbulent jet, but should apply to $Sc \gg 1$ mixing in turbulent shear flows in general. In this sense, we believe that many features of the fine structure seen in our data are generic to mixing at the small scales in all high Reynolds number turbulent flows.

2.1 *Laser diagnostics*

The experiments use a laser induced fluorescence imaging system specifically designed for very highly resolved, three- and four-dimensional, spatio-temporal measurements of the full space- and time-varying conserved scalar field $\zeta(\mathbf{x},t)$ and the associated scalar energy dissipation rate field $\nabla\zeta\cdot\nabla\zeta(\mathbf{x},t)$ in a turbulent flow. Each measurement produces the scalar field at over 3 billion individual points in space and time. The resulting gigabyte-sized data sets are structured as shown in Fig. 1. Each such measured data space consists of a rapid succession of individual three-dimensional spatial data volumes. Each of these data volumes is itself composed of a sequence of two-dimensional spatial data planes, which in turn consist of an array of 256 $\times$ 256 data points. The spatial separation between adjacent points within each data plane, and between adjacent data planes within each data volume, is smaller than the local strain-limited

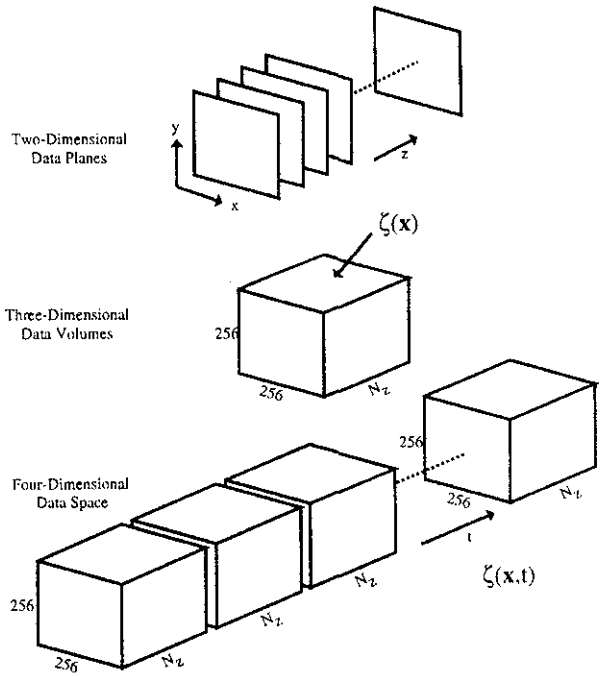

FIG. 1. Structure of the four-dimenional data space which consists of temporally connected three-dimensional data volumes. Each data volume is comprised of a series of spatially connected two-dimensional data planes which are in turn made up of a square array of 256 $\times$ 256 pixels. The final data space can have over 3 billion point measurements of the conserved scalar field.

molecular diffusion lengthscale λ_D of the scalar field. Similarly, the temporal separation between adjacent data planes within each data volume, and between the same data plane in successive data volumes, is shorter than the local molecular diffusion scale advection time $\lambda_D/\overline{u}$, where $\overline{u}$ is the mean velocity for the measurement location (Wygnanski & Fiedler 1969).

Key elements of the imaging and data acquisition system assembled for these three- and four-dimensional measurements are shown schematically in Fig. 2. This system is described in more detail in Dahm *et al* (1991). Briefly, a pair of very low inertia, galvanometric mirror scanners are used to sweep a collimated laser beam in a raster pattern through the desired spatial volume in the flow. The ramp signals driving these mirror scanners are slaved to the same master clock that drives the imaging array, thus insuring that each sweep of the beam corresponds to a single data plane. One scanner provides the (fast) vertical sweep in the x-y plane, while the second creates the (slower) horizontal sweep in the z-direction. Depth of field considerations set the aperture limit on the imaging lens. The resulting laser induced fluorescence intensity is measured with a 256 × 256 element photodiode array with center-to-center pixel spacing of 40μm. This array can be driven at variable pixel rates up to 11 MHz. The fluorescence output from the array is digitized to 8-bits, and then ported into a 16 MB buffer from which is continuously written in real time to a 3.1 GB high-speed parallel transfer disk rank. The overall sustained data throughput rate to the disks is up to 9.3 MB/sec. The 3.1 GB disk capacity can accommodate more than 50,000 such 256 × 256 spatial data planes.

2.2 *Resolution*

The present measurements were obtained at an axial location 235 jet momentum diameters (1.15 m) downstream of the jet source and a radial location 13 cm off the jet centerline (half-way along the jet radius). To estimate the resulting resolution requirements, we note that $\delta(x) \approx 0.44 \cdot x$ and $u(x) \approx 7.2\,(J/\rho)^{1/2} \cdot x^{-1}$, with J the jet source momentum flux and ρ the ambient fluid density. At the outer scale Reynolds number of 3,700 and with the Schmidt number of 2075, these scalings give the local strain-limited molecular diffusion lengthscale estimate of $\lambda_D \approx 257$ μm and the local advection time scale estimate of $(\lambda_D/\overline{u}) \approx 113$ msec at the location of the measurement volume, where $\lambda_D = 11.2 \cdot \delta \cdot Re_\delta^{-3/4} \cdot Sc^{-1/2}$ (Buch & Dahm 1991). With the measurements having an image ratio of

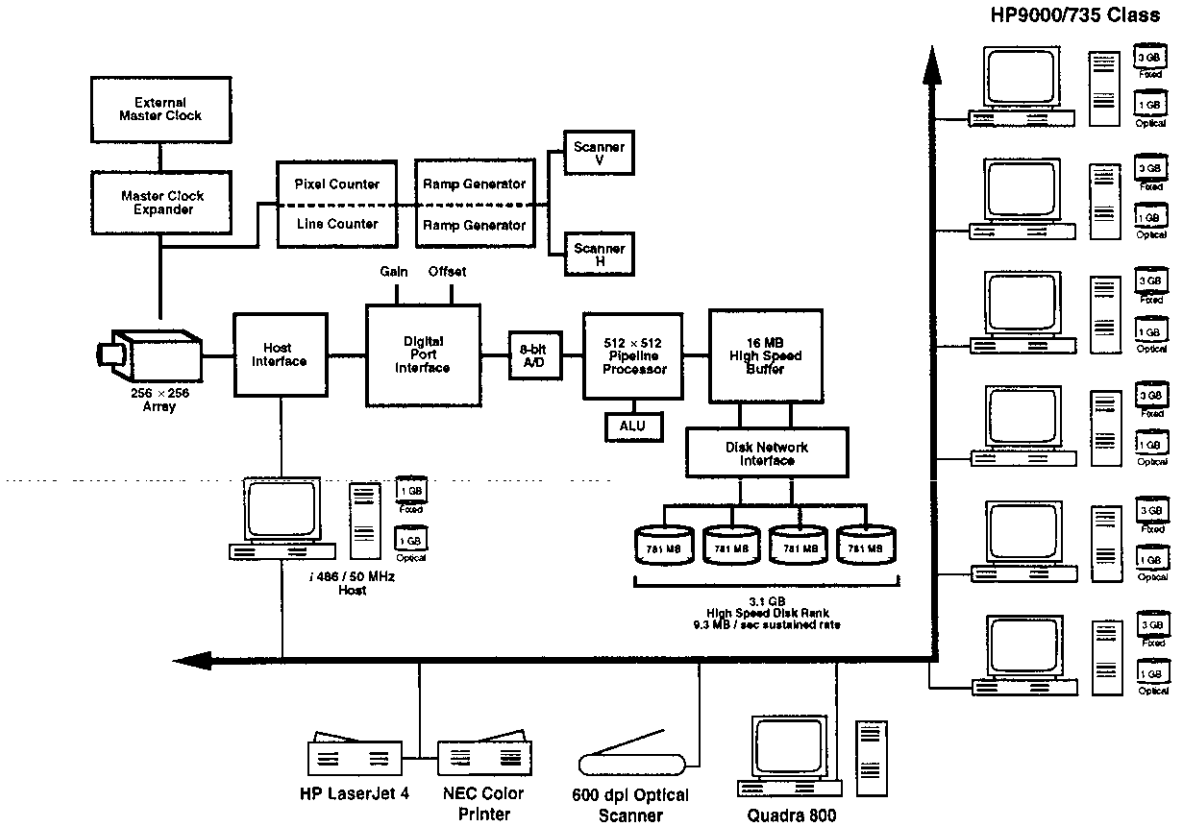

FIG. 2. Key elements of the high-speed variable rate imaging and data acquisition system assembled for these highly resolved four-dimensional measurements of scalar mixing in turbulent flows. Two low-inertia galvanometric mirror scanners are slaved to the imaging array timing to rapidly sweep the laser beam in a succesive raster scan fashion through the scalar field. The data acquisition system can achieve a sustained data throughput rate to the disk rank of up to 9.3MB/sec for volumes as large as the full 3.1 GB disk capacity.

2.72, the in-plane spatial resolution was $\Delta(x,y) \approx 109\ \mu m$. The ($1/e$) laser beam thickness was measured as 270 μm. Deconvolution of the scalar field measurements among adjacent planes increases the effective spatial resolution in the z-direction to the interplane separation $\Delta z \approx 120$ μm between successive data planes. Comparing these Δx, Δy and Δz values with λ_D allows assessment of the relative spatial resolution achieved. In particular, both the resulting pixel image volume $(\Delta x \cdot \Delta y \cdot \Delta z)^{1/3}$ and its maximum dimension (Δz) are more than 2 times smaller than λ_D. Similarly, the temporal separation between successive data planes was $\Delta t = 8.6$ msec, which can be compared with the local diffusion scale advection time of 113 msec. As a result, the present measurements should be capable of resolving essentially all of the fine scale structure of the local turbulent mixing process.

3. Sample Data

The scalar field data are obtained in both three-dimensional (spatial) and four-dimensional (spatio-temporal) form, depending on the number of z-planes chosen for each data volume. In the former, data for $\zeta(\mathbf{x},t)$ throughout each of the nominally 256^3 spatial volumes are simultaneously differentiable in x, y, and z. In the latter, spatial volumes with fewer z-planes, the $\zeta(\mathbf{x},t)$ data are differentiable in x, y, z, and t and thus the volumes are more closely spaced in time. Note that, in both cases, time resolution is maintained as noted above. However, for the purposes of this paper, time differentiability is not essential for any of the results to be presented. We therefore focus on analyzing data in three-dimensional spatial data volumes of the type shown in Fig. 3*a,b*. Each such volume consists of over 16 million individual data points on a regular 256^3 spatial grid. For the chosen coordinate frame, the x axis points outward along the jet radius, the y axis points along the upstream direction, and z points in the azimuthal direction following a right-handed convention. Owing to the fully-resolved three-dimensional nature of these scalar field data, together with the high signal quality attained, accurate differentiation is possible in x, y and z to obtain the scalar gradient vector field $\nabla\zeta(\mathbf{x},t)$ throughout each volume. Of interest for mixing applications is the corresponding scalar energy dissipation rate field $\nabla\zeta \cdot \nabla\zeta(\mathbf{x},t)$, giving the local instantaneous rate at which the scalar energy $\frac{1}{2}\zeta^2(\mathbf{x},t)$ is being reduced by molecular diffusion in the flow. Fig. 4*a,b* shows the scalar dissipation fields obtained for these same two spatial data volumes. These are obtained by direct linear central differencing on a $3 \times 3 \times 3$ template in the scalar field. Beyond the filtering effect implicit in this (or any other) discrete derivative template, no explicit smoothing or filtering is applied to any of these fields. A closer view of these scalar dissipation fields in one of these volumes is given in the individual planes of Fig. 5.

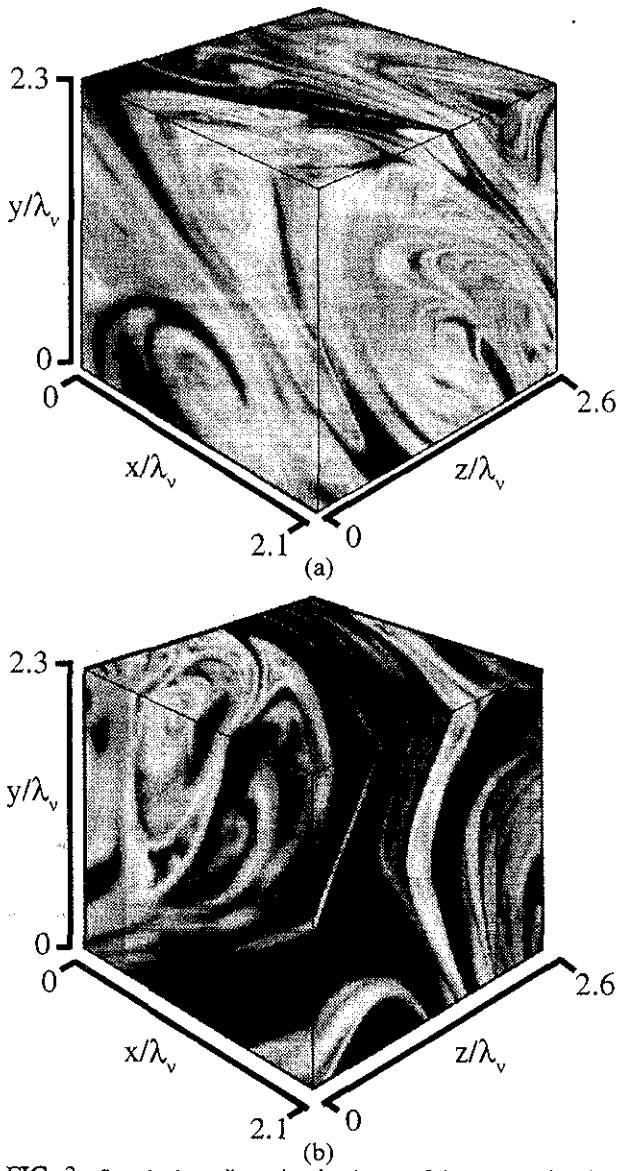

FIG. 3. Sample three-dimensional volumes of the measured scalar field in the far-field of an azisymmetric jet with Re=3700 and Sc=2075. The two volumes shown are temporally separated within the full four-dimensional data space with (a) corresponding to volume #39 and (b) to volume #77. Red denotes the highest scalar value seen in the volume while blue represents pure ambient fluid entrained within the jet.

The dissipation fields in Figs. 4 and 5 are shown in both linear and logarithmic mappings. The linear mapping clearly demonstrates the relatively infrequent occurrence of high rates of molecular mixing, while the logarithmic mapping better reveals the layer-like structure in the dissipation fields. Our previous work has focused on the physical-space structure of these dissipation layers, and their implications for modeling molecular mixing and chemical reactions in turbulent flows. Here we will focus in part on the spectral signature of these layers in the high wavenumber part of the scalar fluctuation spectrum.

Each measurement of this type produces a temporal sequence of more than 150 such three-dimensional spatial data volumes, spanning slightly more than three local outer scale times (δ/u). We typically analyze data from every third such volume to reduce the computational load involved to a manageable level and avoid repetition of scalar field information. This appears adequate to extract essentially all the statistics from each of the data sets, however the relatively small number of outer time scales spanned by each of these precludes full convergence of the temporal statistics of the scalar field. In principle this requires analysis of data from, say, three or more data sets at a given condition in order to obtain reasonably converged statistics. The results presented here are from a preliminary analysis of 29 data volumes at $Re_\delta \approx 3700$. The point-to-point spacing in the x and y directions in this case is 108.8 μm, and the interplane spacing is 120 μm, with the estimated diffusion lengthscale being 257 μm. This case is chosen for detailed analysis since it offers the highest resolution of the data collected to date. Note that the data volumes are stripped down to 223 × 249 × 254 points in the x, y, and z directions respectively to remove edge pixels deemed to have unreliable response. Analyses are performed on only these central points within each volume.

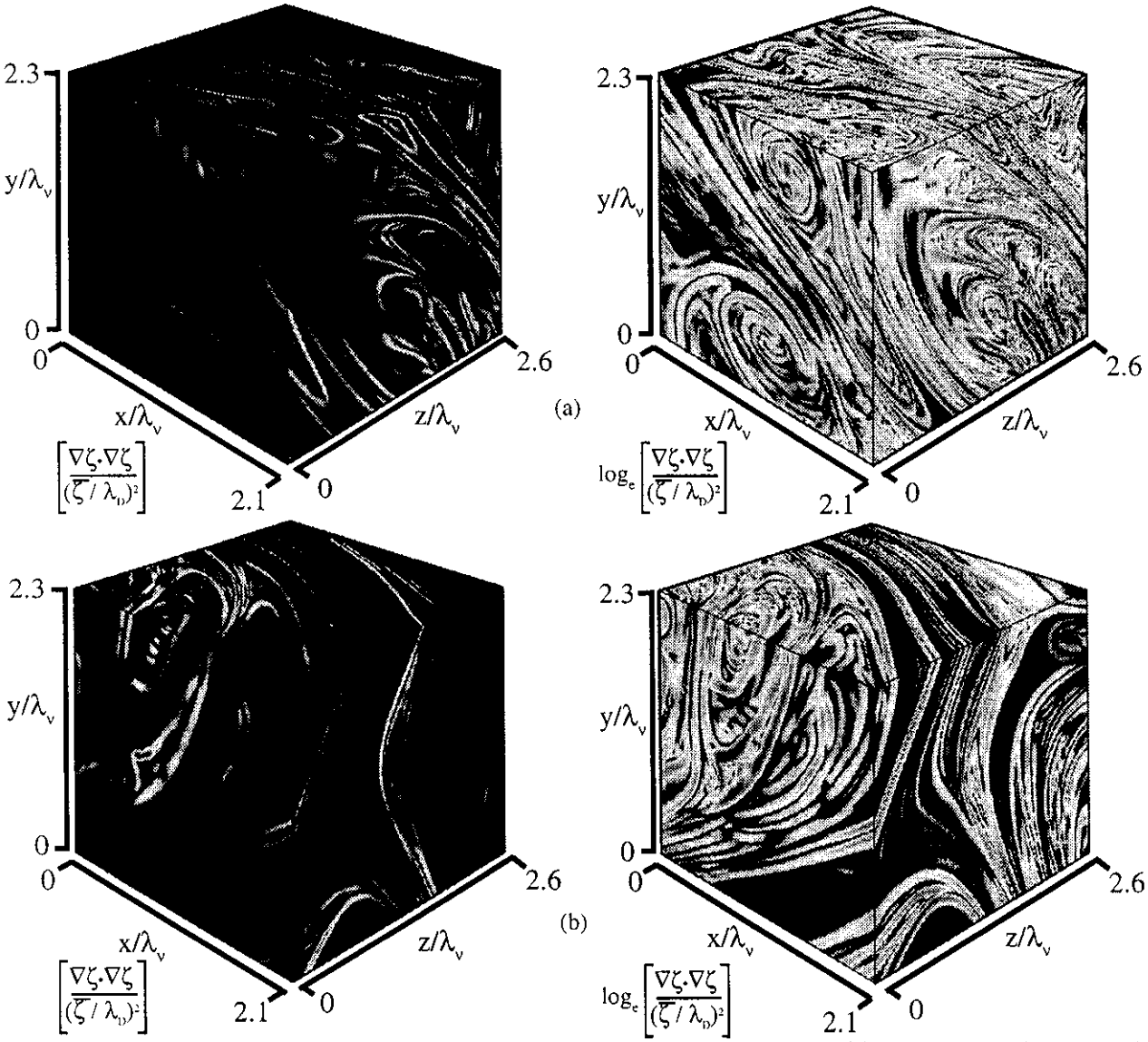

FIG. 4. The scalar dissipation fields resulting from direct differentiation in all three spatial directions of the scalar volumes of fig. 3. Data is presented as $\nabla\zeta\cdot\nabla\zeta(\mathbf{x},t)$ on the left and $\log_e(\nabla\zeta\cdot\nabla\zeta(\mathbf{x},t))$ on the right. As in figure 3, (a) above corresponds to volume #39 and (b) below to volume #77 within the full four-dimensional data space comprised of as many as 180 such volumes. The cubes on the left reveal the infrequency of high molecular mixing rates while those on the right reveal a layer-like structure for all levels of dissipation.

4. Scalar Field Statistics

We first present results for single-point statistics of the conserved scalar and scalar dissipation fields in the self-similar jet far field. Such single-point scalar field statistics in turbulent jets have been reported from a number of previous investigations (e.g. Wygnanski & Fiedler 1969; Antonia, Prabhu & Stephenson 1975; Becker, Hottel & Williams 1967; Birch *et al* 1978; Chevray & Tutu 1978; Lockwood & Moneib 1980). These allow comparisons and partial validation of the measurements, however it must be kept in mind that the resolution in the present data is higher than in any prior investigation. It is thus equally interesting to look for differences that may be attributable to the higher resolution. Also, measurements of scalar field statistics for large *Sc* scalar mixing in jets are comparatively few. Moreover, unlike most previous measurements of scalar dissipation and scalar gradient statistics, the present results are obtained from simultaneous measurements of all three scalar gradient vector components, and thus do not require any Taylor hypotheses or assumptions of isotropy. Two-point statistics, in the form of scalar field spectra, are presented in §5.

Figure 6 shows the probability density function (pdf) of the conserved scalar ζ at the (r/x) = 0.11 measurement location. [Note that this radial location is at the point where the scalar fluctuation level is highest; e.g. see Wygnanski & Feidler 1969]. Both the shape and width of this pdf are interesting. Notice first the strong spike near $\zeta = 0$, corresponding to near-ambient fluid concentration levels. The area under this spike accounts for a significant fraction of the pdf – over 11% of the fluid at this radial location in the far field is at concentrations less than one-tenth of the local mean value. Previous measurements of the pdf along the jet radius for *Sc* » 1 scalar mixing also show an ambient fluid spike at this location, however in those cases the spike accounted

0 (a) $\zeta/\overline{\zeta}$ 3.5

0 (b) $\dfrac{\nabla\zeta\cdot\nabla\zeta}{(\overline{\zeta}/\lambda_D)^2}$ 2.0

−3.9 (c) $\log_e\left[\dfrac{\nabla\zeta\cdot\nabla\zeta}{(\overline{\zeta}/\lambda_D)^2}\right]$ 0.80

FIG. 5. Two-dimensional cuts through volume #39 revealing some of the interior data of the cubes in figs. 3 and 4. (a) gives a slice of the scalar field which spans approximately two vorticity diffusion scales in both the outward radial and the upstream directions. Its corresponding scalar dissipation fields are shown in linear form in (b), and in logarithmic form in (c). The color bar above gives the numerical values associated with each color and image.

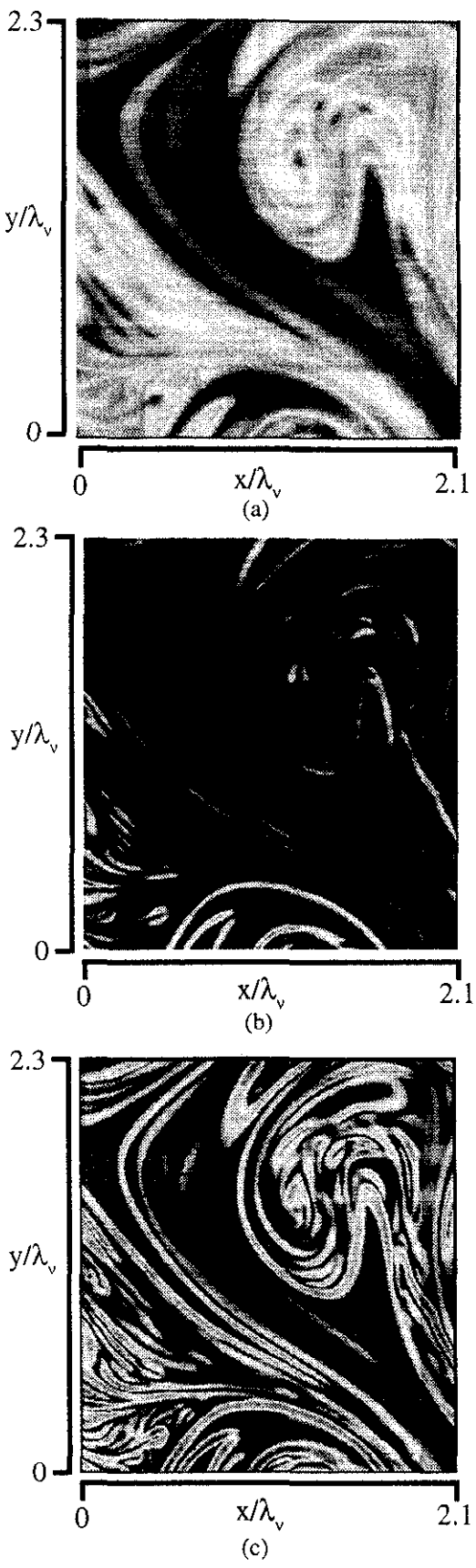

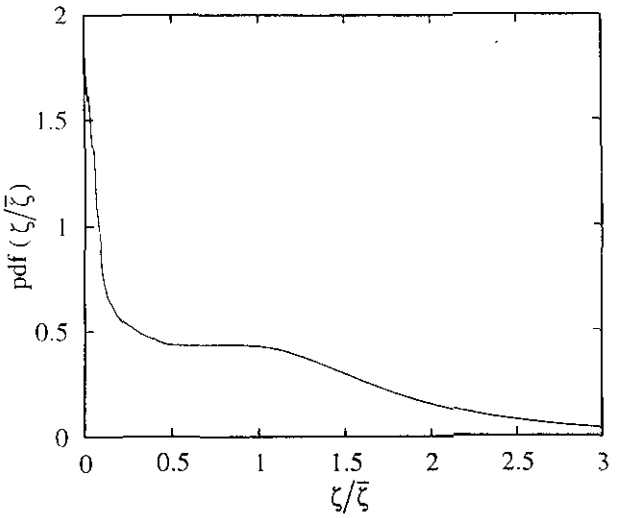

FIG. 6. Probability density of the conserved scalar in the far field of an axisymmetric jet with a Reynolds' number of 3700 and a radial location of r/x = 0.11, or 13 cm from the jet centerline.

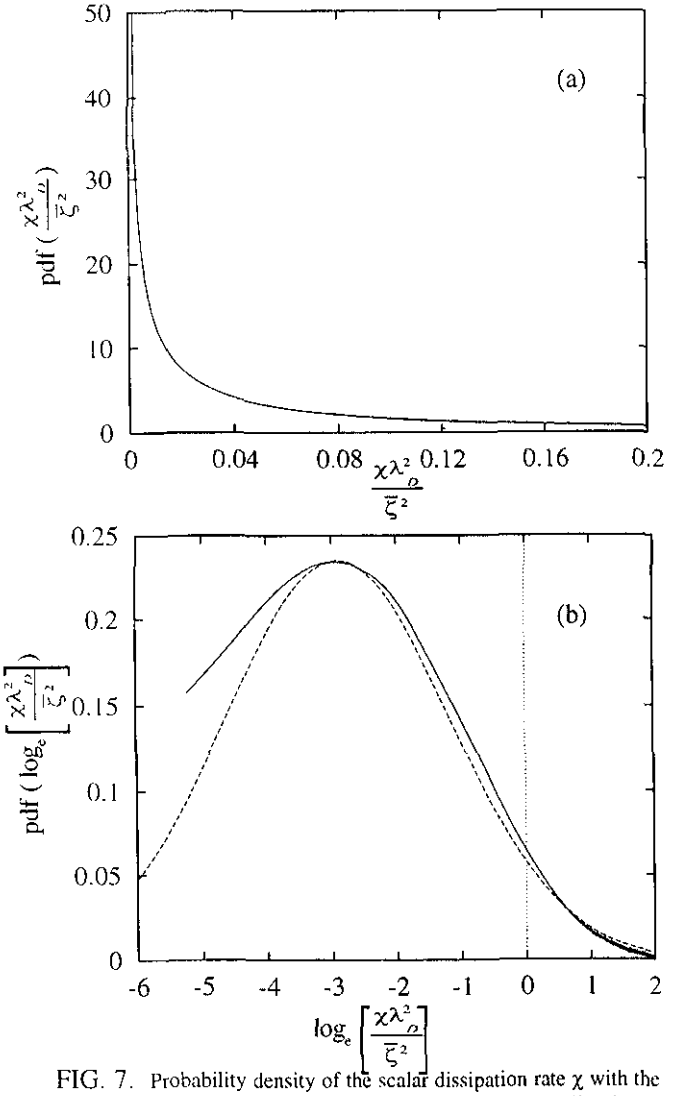

FIG. 7. Probability density of the scalar dissipation rate χ with the same conditions as those of fig. 4. (a) gives the pdf(χ) while (b) reveals the pdf($\log_e\chi$). Also shown in (b) is a gaussian curve, representing a lognormal distribution for pdf(χ), fit to the pdf above $\log_e\chi^*$=–3.

for a significantly smaller fraction of the fluid. In fact, the entire pdf in Fig. 6 has a noticeably different shape than do results reported from previous investigations for large *Sc* mixing. These differences appear directly attributable to the lower spatial resolution of earlier investigations. In particular, prior measurements of the pdf show a broad peak centered near the local mean value, with a small spike near the ambient fluid value. The present result show no peak near the mean value, and show more fluid at extremely low and high concentrations than has been suggested by results reported to date. The most highly resolved of prior measurements (Dahm & Dimotakis 1987, 1990) give the maximum scalar concentration normalized by the local mean at this radial location as 2.4, whereas we find a significant fraction of the scalar values above even three times the local mean. Consistent with this difference in the maximum values, prior measurements of $Sc \gg 1$ scalar fluctuation levels in turbulent jets showed a normalized scalar variance at this radial location no higher than 0.68 (Antonia *et al* 1975). By comparison, the second moment of the pdf in Fig. 6 gives the normalized variance as 0.88. These observations suggest that the pdf in Fig. 6, based on these highly resolved measurements, properly reflects the true distribution of scalar values at this radial location in the jet far field. Note, however, that while this shape is significantly different than previous lower-resolution measurements may have suggested, it nevertheless still appears reasonably representable by the β-function family of shapes commonly used in assumed-shape pdf models of scalar mixing.

The availability of scalar field information in all three spatial dimensions allows determination of the true scalar energy dissipation rate field, and hence allows measurement of the probability density of this quantity. Unlike previous measurements, no assumption of isotropy needs to be made to convert a lower-dimensional estimate into the true three-dimensional scalar gradient. Similarly, the spatial nature of these measurements allows direct evaluation of spatial derivatives, in contrast with time series measurements that require a Taylor hypothesis to estimate spatial derivative components. In Fig. 7*a* we show the probability density of the true scalar energy dissipation rate $\chi \equiv (ReSc)^{-1}\nabla\zeta\cdot\nabla\zeta$. Note that, as can be seen from the dissipation fields in Fig. 4, most of the values are concentrated near the low dissipation end, with high dissipation rates being rare. This intermittent character of the dissipation fields in turbulent flows has been known since the earliest measurements of Batchelor & Townsend (1949). Classical theories of turbulence (e.g. Kolmogorov 1962) suggest a lognormal distribution for dissipation variables to account for this intermittency. Accordingly, in Fig. 7*b* we show the probability density of $log_e\ \chi$,

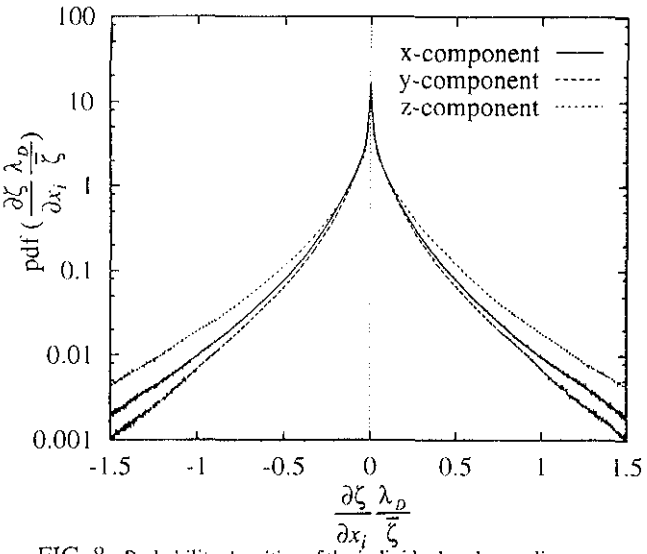

FIG. 8. Probability densities of the individual scalar gradient components in the x-direction (outward radial), y-direction (upstream), and z-direction (azimuthal).

together with a true lognormal distribution having the same first and second moments. Note that, owing to the limited digital resolution of the measurements, the range of dissipation rates that can be distinguished does not allow accurate assessment of the distribution at low values. However, for higher values it can be seen that the lognormal distribution gives a fair fit, though significant differences are discernible. While accurate determination of the complete pdf of χ is currently of considerable interest, and has important implications for validation of alternative descriptions of turbulence, the 8-bit signal depth of the present measurements does not permit more precise statements than in Fig. 7. We choose therefore to focus instead on the three-dimensional spatial information offered by these data.

Figure 8 shows the probability densities for the individual spatial derivatives in the three orthogonal directions that make up the local scalar gradient and the associated scalar dissipation. These in turn reflect the degree of isotropy at the small scales in the scalar field. In particular, for an isotropic scalar field, the scalar gradient vector has no preferred orientation, and thus the distributions for all three gradient vector components will be identical. It is apparent in Fig. 8 that the distributions are largely similar, though there are differences discernible (it must be kept in mind that the axes are semi-logarithmic). Moments of each of these distributions show that the mean-square gradient in the x, y, and z directions are respectively, 0.039, 0.031, and 0.060 when normalized with the molecular diffusion scale and the mean scalar value. The differences in the x and y components are likely to be a result of genuine anisotropy, as discussed below. However, the significantly higher gradients in the z-direction are likely to be a result of the slewing between successively acquired planes in the three-dmensional data volume. Small but unavoidable motion in the scalar field between successive z-planes leads to an enhancement of the z-derivative component. Other manifestations of this slewing will be seen in results presented below. Note that it is possible to partly correct the z-derivative to account for this slewing in the four-dimensional data. In particular, if the local velocity were known, then the z-derivative could be exactly corrected. Lacking the velocity required for this, a partial correction can be based on the local mean velocity, however, this is not implemented here.

The final feature of interest in Fig. 8 is the scaling of the tails of these distributions at very large positive and negative derivative values. Unless these tails are exponentially decreasing, moments of the distribution above some order will become divergent. Exponential tails will appear as straight lines in these semi-logarithmic axes.

Since the scalar dissipation fields in Figs. 4 and 5 result from direct differentiation of the scalar fields in Fig. 3, simultaneous conserved scalar and dissipation rate information is available at each point. This allows the joint probability density between these two variables to be directly constructed. Figure 9 shows the joint distribution resulting from these measurements. The contour values increase logarithmically, with each being twice that of the one above it. Again, no assumptions of isotropy are involved. The result shows that the scalar and scalar dissipation rate are essentially statistically independent. Perhaps more importantly, this joint distribution allows the conditional dissipation $\langle\chi|\zeta\rangle$, which is central to conditional moment closure models of reacting turbulent flows, to be evaluated. Note also that this joint pdf reveals that points in the flow with high and

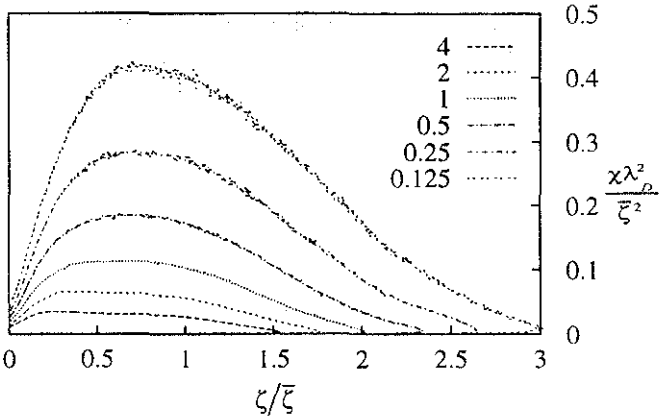

FIG. 9. Joint probability density function between the conserved scalar ζ and its corresponding scalar dissipation rate χ. Contours vary logarithmically with each one having twice the value of the one above it.

low values of the conserved scalar tend to have low dissipation rates, while the greatest dissipation rates occur most frequently at points with approximately 80% of the mean scalar value. This appears to be in good agreement with the results of Anselmet & Antonia (1985), who estimated the joint pdf for this pair of variables in the far-field of a turbulent planar jet and found the contours to peak slightly below the mean temperature.

A different view of the anisotropy in the scalar gradients is shown in Figs. 10*a*,*b*. This gives the probability densities for the two spherical angles ϑ and φ describing the vector orientations in the gradient field $\nabla\zeta(\mathbf{x},t)$. Here ϑ measures the angle from the (positive) x-axis of the vector projection into the x-y plane, while φ measures the angle between the gradient vector and the (positive) z-axis, so that

$$\vartheta \equiv \tan^{-1}\left(\frac{\partial\zeta/\partial y}{\partial\zeta/\partial x}\right) \qquad (1a)$$

$$\varphi \equiv \cos^{-1}\left(\frac{\partial\zeta/\partial z}{|\nabla\zeta|}\right) \qquad (1b)$$

In an isotropic scalar field, the probability density of ϑ values will be uniform at $(2\pi)^{-1}$, while the spherical geometry requires φ to be sinusoidally distributed as $1/2\sin(\varphi)$. These isotropic distributions are also shown in Fig. 10. Figure 10*a* shows that, for the data represented here, the ϑ distribution has peaks at $\vartheta \approx 0$ and $\vartheta \approx \pi$, suggesting slightly more gradient vector content in the x-derivatives than in the y-derivatives. It is known that the pixel rows and columns in the array have slightly different characteristics. These peaks however account for only slightly more than 5 percent of the total probability. It is also apparent that there is a smaller peak in the direction of the most compressional mean strain axis, namely $\vartheta \approx -41^\circ$ and 139°. In addition, a minimum is seen in the direction of the most extensional principal strain axis of the mean flow strain field at this radial location in the jet, namely $\vartheta \approx 49^\circ$ and also diametrically opposite. Note also in Fig. 10b that the distribution of φ values shows a dip away from its isotropic form near $\pi/2$, so that the gradient vector has a disproportionate tendency not to lie in the x-y plane. It appears likely that this is a manifestation of the slewing between adjacent data planes. The slight motion of the flow between the acquisition of one plane and the next causes an artificial gradient to be produced in the z-direction if the local velocity vector points significantly in the direction of the local scalar gradient vector. Motion perpendicular to the scalar gradient will have little effect on the measured z-derivative component.

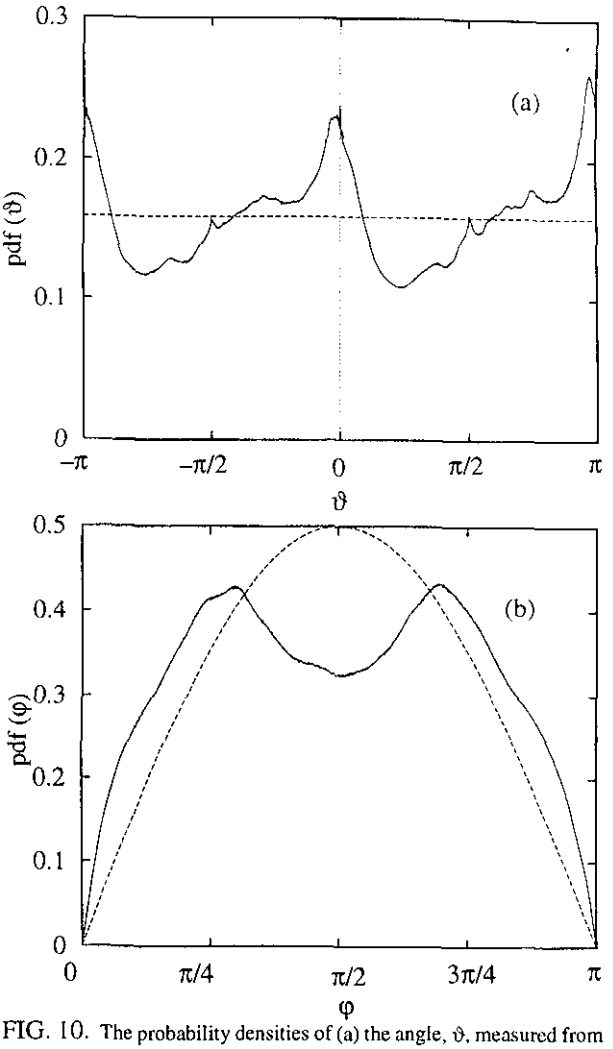

FIG. 10. The probability densities of (a) the angle, ϑ, measured from the positive x-axis and formed by the projection of the full three-dimensional scalar gradient vector into the x-y plane and (b) the angle between the scalar gradient vector and the positive z-axis, φ. An isotropic arrangement of the scalar gradient vector would lead to pdf $(\vartheta)=1/(2\pi)$ and pdf$(\varphi)=1/2\sin(\varphi)$.

5. Spatial Spectra

For locally homogeneous and isotropic turbulence at Reynolds numbers sufficiently high to allow an inertial subrange, classical turbulence theory suggests that the spatial spectrum of the kinetic energy field in the inertial range will follow a $k^{-5/3}$ power law scaling. Similar arguments and dimensional reasoning can be applied to the scalar spectrum, and measurements show that this spectrum also follows, at least approximately, a $k^{-5/3}$ power law form in the inertial range as well (Gibson and Schwartz 1963; Grant, Hughes, Vogel, and Moillet 1968). For yet higher wavenumbers, Batchelor (1959) argued that, when $Sc \gg 1$, owing to the disparate dissipative scales λ_v and λ_D in the scalar and kinetic energy fields, the scalar spectrum should follow a k^{-1} form in the range of wavenumbers $k_v \ll k \ll k_D$ where $k_v \equiv 2\pi/\lambda_v$ and $k_D \equiv 2\pi/\lambda_D$. For wavenumbers on the order of k_D and higher, the theory

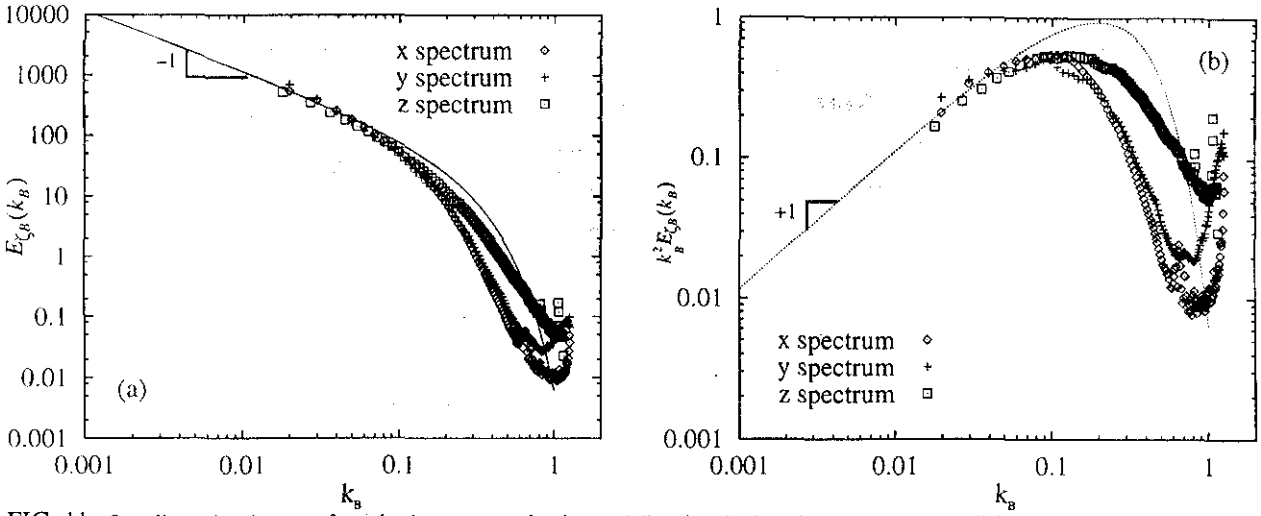

FIG. 11. One-dimensional spectra from the three measured orthogonal directions in the axisymmetric jet, x (radially outward), y (upstream), and z (clockwise) presented as (a) the scalar energy spectra and (b) the dissipation spectra. Overlayed is Batchelor's equation for the scalar spectrum of high wavenumber mixing given in (2) for q=5.

suggests an exponential roll-off as the scalar energy is dissipated. Batchelor's resulting theoretical function for the one-dimensional scalar spectrum at high wavenumbers can be written in the notation of Williams & Paulson (1977) as

$$E_\zeta(k/k_B) = \frac{4\pi^{1/2} q^{3/2} D^{1/2} \overline{\chi}}{(\varepsilon/\nu)^{3/4}} \left[\frac{N(B)}{B} - \int_B^\infty N(y)\,dy \right] \quad (2)$$

Here $\overline{\chi}$ is the measured scalar energy dissipation rate, ε is the kinetic energy dissipation rate (here estimated from measurements in turbulent jets by Taulbee, Hussain, & Capp (1987)), and ν and D are the diffusivities of the vorticity and the scalar, respectively. $N(B)$ is the normal distribution given by $(2\pi)^{-1/2}\exp(-\frac{1}{2}B^2)$ where $B = (2q)^{1/2}\, k/k_B$. k_B is the characteristic wavenumber of the Batchelor scale and q is a constant that relates the magnitudes of the principal rates of strain. Batchelor suggested that this universal constant should be two, but subsequent experimental investigations have suggested values as high as six (Williams & Paulson 1977).

In addition to these one-dimensional spectra, the three-dimensional spatial nature of data such as those shown in Figs. 3-5 allows the full three-dimensional spatial scalar spectrum $E_\zeta(\mathbf{k})$ to be obtained. Such measurements have not previously been possible. Moreover, the three-dimensional spatial scalar spectrum then allows determination of the spherical spectrum $E_\zeta(k)$, obtained by integration over spherical shells centered around the origin in three-dimensional wavevector space. For homogeneous isotropic turbulence, the relationship between this one-dimensional spectrum estimation and its isotropic spectrum function denoted $E_\zeta(k)$ is (e.g.

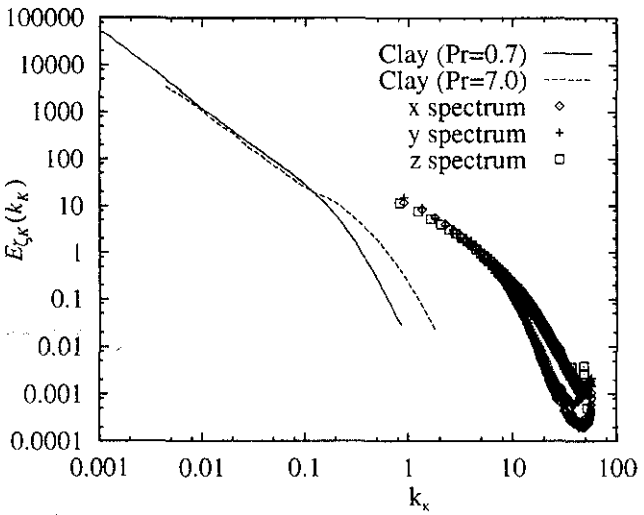

FIG. 12. Comparison of the one-dimensional spatial spectra within a jet of Re=3700 and Sc=2075 with that of the temporal spectra of Clay(1973). The Pr=0.7 curve resulted from a heated air jet of Re=100,000 and the Pr=7.0 curve came from temperature measurements in the wake of a sphere, Re=27,600. The data is presented in Kolmogorov normalized coordinates

Tennekes & Lumley 1972)

$$E_\zeta(|\mathbf{k}|) = k^3 \frac{d}{dk}\left(\frac{1}{k}\frac{dE_{\zeta_{1D}}}{dk}\right) \quad (3)$$

Collapsing the three-dimensional spectrum into its three one-dimensional spectra allows an isotropy test through this equation. Note from (3) that any power law scaling k^p in the one-dimensional spectrum will remain unchanged in the corresponding isotropic spectrum function $E_\zeta(k)$.

The results presented below for these various scalar spectra were obtained using an FFT algorithm (Press, W.

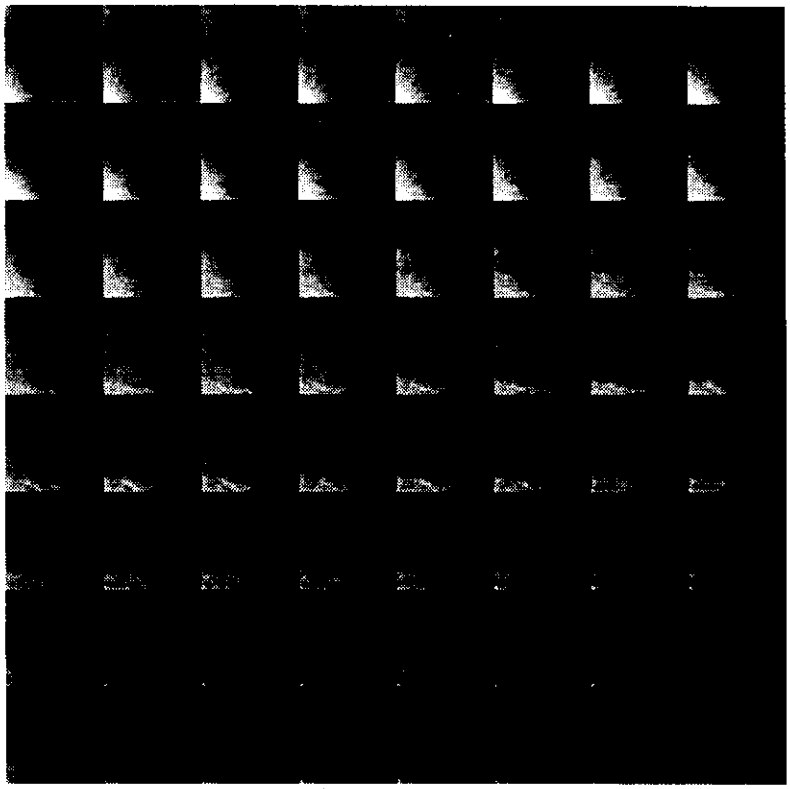

FIG. 13. The full three-dimensional scalar energy spectrum in a turbulent jet ensemble averaged over 232 volumes of data, each consisting of 128×128×128 point measurements of the conserved scalar field. The full result is displayed with k_z varying between each of the 64 images seen here and k_x and k_y varying within each image. k_z has the value zero in the upper left-hand image and increases from left to right and then top to bottom so that the maximum frequency in the z-direction is represented in the lower right-hand image. k_x varies from right to left and k_y from bottom to top within each of the 64 images of constant k_z. The magnitude of the scalar energy spectrum at each data point is color coded (in color versions) logarithmically decreasing from red to blue with six decades inbetween the two colors.

H. et al 1992). The one-dimensional data were prepared for the transform by first subtracting the mean to remove the offset, followed by the subtraction of a least-squares fit parabola, and finally by windowing the data records with a Hanning window. The data are typically presented in terms of the Kolmogorov-normalized scalar spectrum. This normalization is outlined carefully by Gibson (1968) and essentially consists of dividing the resulting spectrum by the square of the Kolmogorov scalar scale and the Kolmogorov length scale, namely

$$E_{\zeta_K}(k) = \frac{E_\zeta(k)}{\Sigma_K^2 \lambda_K} \tag{4}$$

Here $\Sigma_K^2 = \overline{\chi}(\nu/\overline{\varepsilon})^{1/2}$ is the square of the Kolmogorov scalar scale and λ_K is the Kolmogorov length scale equal to $(\nu^3/\overline{\varepsilon})^{1/4}$, estimated as 2.0 mm from the dissipation measurements of Taulbee *et al* (1987) at this radial location in the self-similar far field of axisymmetric turbulent jets. Note that the spectrum $E\zeta(k)$ has the characteristic that

$$\overline{\zeta^2} = \int_0^\infty E_\zeta(k)\,dk \tag{5}$$

and that the wavenumber used here is normalized by the Kolmogorov length scale in the form of $k_K \equiv k\,\lambda_K$.

Results are shown in Fig. 11*a* for the three one-dimensional spectra obtained independently in the x, y, and z directions. Also shown in this figure is Batchelor's spectrum in (2) for $q = 5$. In Fig. 11*b* the same results are presented as isotropic dissipation spectra, where the k^{-1} Batchelor scaling becomes k^1. Note that, owing to the nominally 256^3 points in each spatial data volume, the range of wavenumbers covered by the results is necessarily narrow. Moreover, since the emphasis in these measurements has been on high resolution, much of the range of wavenumbers accessible from these data lies deep in the dissipation range. Nevertheless, some limited insights about the possible validity of Batchelor's spectrum are possible. In particular, while there is some weak indication of possible asymptotic approach to a k^{-1} scaling in Fig. 11*a*, the peak in the dissipation spectrum in Fig. 11*b* allows an asymptotic approach to this power law scaling at lower wavenumbers to be more readily seen. In the latter case, there appears to be a definite approach to the k^1 scaling that supports Batchelor's power law regime. The agreement with $q = 5$ in the dissipation range is, however, not very good. Moreover, while all three

one-dimensional spatial spectra in these figures appear to asymptote to the Batchelor spectrum at the lowest wavenumbers, there are large disparaties between them in the dissipation range. Notice that the x and y spectra are in relatively good agreement with one another except at the very highest wavenumbers where various noise sources dominate. Indeed, the data are known to typically be slightly noisier in the y-derivatives than in the x-derivatives, and this shows in the corresponding spectra. [Note that, while spectral results are often shown truncated above their spectral noise limit, we present the full spectra to allow identification of the different noise patterns inherent in them.] The z-spectrum in Fig. 11, however, contains considerably more high-frequency content. It appears likely that this is at least in part due to the slewing mentioned previously. The artificial z-gradient this introduces will contain a wide range of frequencies. As also noted previously, it may be possible to partly correct for this artificial gradient, though this has not been done in the results presented here. Lastly, the three one-dimensional spatial spectra are compared with Clay's (1973) temporal spectrum results for Sc = 7 and 0.7 in Fig. 12. The Sc = 7 spectrum is a result of temperature measurements in the wake of a sphere at a Re = 27,600, while the Sc = 0.7 spectrum results from measurements within a heated air jet with a much higher Reynolds' number of 100,000. The spacing between the spectra in Fig. 12 along the k_K axis is slightly short of the expected $Sc^{1/2}$ dependence and is being investigated.

The three-dimensional spectrum is estimated from the same three-dimensional spatial data volumes as were the one-dimensional spectra. However, in the interest of speed and consistency, the FFT algorithm with no memory swapping was used for the three-dimensional spectrum as well. Limitations on computer memory required reduction of these calculations from nominally 256^3 volumes to 128^3 volumes. Each 256^3 volume is therefore broken down into 8 subvolumes, and a separate spectrum computed for each. The ensemble average of these three-dimensional spectra is shown in the color images of Fig. 13. Each of the 64 images shown represents a slice through the three-dimensional **k** wavevector space for a constant k_Z value. Within each such slice, k_X increases from left to right and k_Y from the bottom to the top of each plane. The wavenumber k_Z in the out-of-plane direction starts at zero in the upper left and increases from left to right and then top to bottom. The color coding gives the value of the three-dimensional spatial scalar energy spectrum $E_\zeta(\mathbf{k})$ throughout the wavevector space. The highest spectral values are color coded red, with logarithmically decreasing values down to blue.

Noise in the three-dimensional spectrum manifests

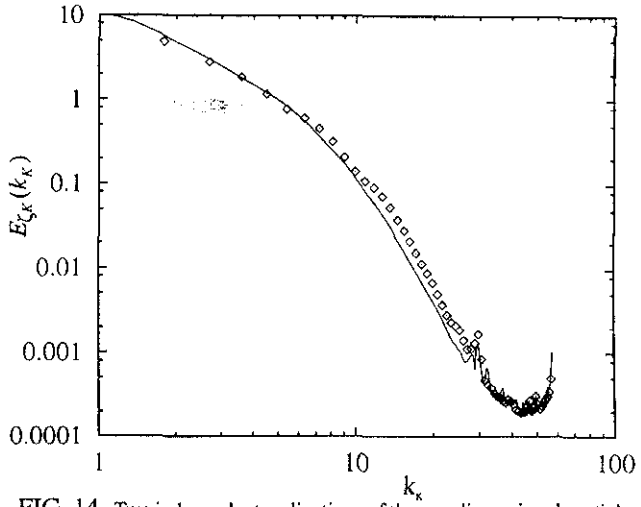

FIG. 14. Two independent realizations of the one dimensional spatial spectrum, calculated in the outward radial direction, are shown for a consistency check. The line represents the direct one-dimensional calculation while the overlayed points result from integration of the full three-dimensional ensemble-averaged spatial scalar energy spectrum.

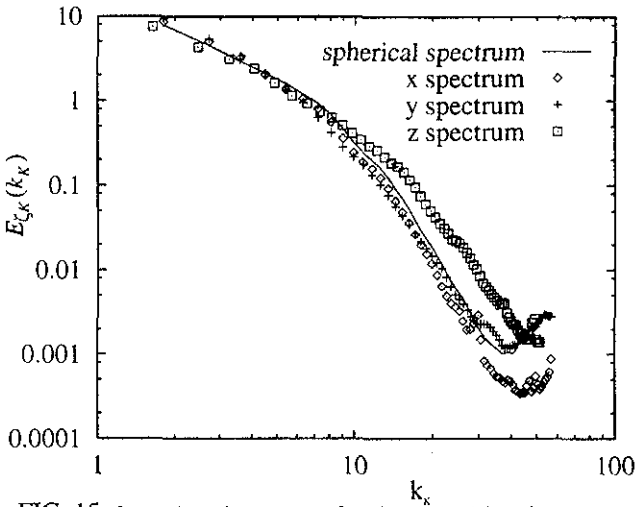

FIG. 15. Isotropic scalar spectrum function derived from integration of the three-dimensional spectrum along spherical shells. Overlayed are the one-dimensional spectra for comparisons.

itself in three minor peaks. One is located at large k_X and small values of the other two components, k_Y and k_Z. The other two peaks occur at the corresponding points in the remaining directions. Noise from the photodiode array has essentially two components, one that causes the signal to vary from row to row, resulting in the peak in k_Y, and one that manifests itself in a column to column variation resulting in the peak in k_X. The temporal aspects of the noise manifest themselves in the z-direction. This noise factor is introduced when the planes, acquired sequentially, are stacked in the z-direction as noted previously. This results in the peak seen in the lower left corner of the bottom right image, where k_Z is large and k_X and k_Y are small. The source of noise that results in the minor peak in the three-dimensional energy spectrum that appears in the center of all 64 planes of constant k_z is currently under

investigation.

The calculated one-dimensional scalar spectrum in any of the three directions is compared for consistency against the spectrum resulting from integration of the full three-dimensional spectrum in the other two directions. Good agreement between the two spectra in the outward radial (or x-) direction can be seen inf Fig. 14. The calculated one-dimensional spectrum is twice as dense as the integrated one and extends to slightly lower frequencies. Perfect agreement is not expected, since due to the overlap in the cubic subsets used to calculate the three-dimensional spectrum, scalar information from some points is used more than others in determining this spectrum.

In addition to integration in the three orthogonal directions, integration of the three-dimensional spectrum over spherical shells in the wavevector space **k** is also possible. Since the full three-dimensional spatial spectrum has not previously been available to any direct experimental measurement, this spherical spectrum has instead been typically calculated under the assumption of isotropy using (3). Here however no such assumption is necessary. Instead we can integrate $E_\zeta(\mathbf{k})$ in Fig. 13 directly over spherical shells in **k** space. This provides information as to the behaviour of the spectrum when the magnitude of the wavevector, and not merely one of its components, is the independent variable. As shown in Fig. 15 the shape of this spectrum very closely matches those of the individual one-dimensional x- and y-directional spectra. All four spectra shown have been normalized via (5), so that the area under each curve is the same and equal to the measured scalar variance.

6. Conclusions

The present results show that experimental measurements of fully-resolved scalar fields with three-dimensional spatial data volumes in turbulent flows at moderate Reynolds numbers are possible. This in turn permits evaluation of the true three-dimensional scalar energy dissipation rate field, without any need for assumptions of isotropy to convert lower-dimensional measurements, and without any need for Taylor hypotheses to convert time measurements to spatial gradients. The resulting data allow relatively detailed studies of the three-dimensional spatial structure in the scalar and scalar dissipation rate fields at the small scales of the flow. The pdf of scalar values shows a shape that differs significantly from previous $Sc \gg 1$ measurements at this radial location in the jet, and these differences appear to be consistent with the higher spatial resolution available in these measurements. There is a strong spike corresponding to near ambient fluid values, and a longer tail extending to higher values than previously measured, with an attendant increase in the true scalar variance. This extended tail also is apparent in the joint pdf of scalar and scalar dissipation. The full three-dimensional spatial scalar spectrum is also accessible to analyses from these measurements. One-dimensional spectra obtained from this show an apparent asymptotic approach in agreement with the k^{-1} Batchelor scaling in the range of wavenumbers $k_v \ll k \ll k_D$.

Acknowledgements

This work is supported by the Air Force Office of Scientific Research (AFOSR) under AFOSR Grant No. 89-0541.

References

Anselmet, F. & Antonia, R.A. (1985) Joint statistics between temperature and its dissipation in a turbulent jet. *Phys. Fluids* **28**, 1048.

Antonia, R. A. & Mi, J. (1993) Temperature dissipation in a turbulent round jet. *J. Fluid Mech.* **250**, 531.

Antonia, R.A., Prabhu, A. & Stephenson, S.E. (1975) Conditionally sampled measurements in a heated turbulent jet. *J. Fluid Mech.* **72**, 455.

Batchelor, G. K. (1959) Small-scale variation of convected quantities like temperature in a turbulent fluid. Part 1. *J. Fluid Mech.* **5**, 113.

Batchelor, G.K. & Townsend, A. A. (1949) The nature of turbulent motion at large wavenumbers. *Proc. Roy. Soc. Lond. A* 199, 238.

Becker, H.A., Hottel, H.C. & Williams, G.C. (1967) The nozzle-fluid concentration field of the round turbulent jet. *J. Fluid Mech.* **30**, 285.

Birch, A.D., Brown, D.R., Dodson, M.G. & Thomas, J.R. (1978) The turbulent concentration field of a methane jet. *J. Fluid Mech.* **88**, 431.

Buch, K. A. & Dahm, W. J. A. (1991) Fine scale structure of conserved scalar mixing in turbulent shear flows: Sc » 1, Sc ≈ 1 and implications for reacting flows, Ph. D. Thesis, The University of Michigan, Ann Arbor.

Chevray, R. & Tutu, N.K. (1978) Intermittency and preferential transport in a round jet. *J. Fluid Mech.* **88**, 133.

Clay, J. P. (1973) Turbulent mixing of temperature in water, air, and mercury, Ph. D. Thesis, University of California-San Diego, La Jolla.

Dahm,W.J.A. & Dimotakis, P.E. (1987) Measurements of entrainment and mixing in turbulent jets. *AIAA J.* **25**, 1216.

Dahm, W.J.A. & Dimotakis, P.E. (1990) Mixing at large

Schmidt number in the self-similar far field of turbulent jets. *J. Fluid Mech.* **217**, 299.

Dahm, W. J. A., Southerland, K. B., & Buch, K. A. (1991) Direct, high-resolution, four-dimensional measurements of the fine scale structure of Sc » 1 molecular mixing in turbulent flows. *Phys. Fluids A* **3**, 1115.

Gibson, C. H. (1968) Fine structure of scalar fields mixed by turbulence. II. Spectral theory. *Phys. Fluids* **11**, 2316.

Gibson, C. H. & Schwartz, W. H. (1963) The universal equilibrium spectra of turbulent velocity and scalar fields. *J. Fluid Mech.* **16**, 365.

Grant, H. L., Hughes, B. A., Vogel, W. M., & Moilliet, A. (1968) The spectrum of temperature fluctuations in turbulent flow. *J. Fluid. Mech.* **34**, 423.

Kolmogorov, A.N. (1962) A refinement of previous hypotheses concerning the local structure of turbulence in viscous incompressible fluid at high Reynolds number. *J. Fluid Mech.***13**, 82.

Lockwood, F.C. & Moneib, H.A. (1980) Fluctuating temperature measurements in a heated round jet. *Comb. Sci. Tech.* **22**, 3.

Press, W. H., Teukolsky, S. A., Vetterling, W. T., & Flannery, B. P., *Numerical Recipes, 2nd Edition* (Cambridge University Press, New York, 1992), pp. 490–529.

Taulbee, Hussain, & Capp (1987) The round jet: experiment and inferences on turbulence modeling, *Sixth Symp. Turb. Shear Flows*, Toulouse, France.

Tennekes, H. & Lumley, J. L., (1972) *A first course in turbulence.* MIT Press, Cambridge, MA.

Williams, R. M. & Paulson, C. A. (1977) Microscale temperature and velocity spectra in the atmospheric boundary layer. *J. Fluid Mech.* **83**, 547.

Wygnanski, I. & Fiedler, H.E. (1969) Some measurements in the self-preserving jet. *J. Fluid Mech.* **38**, 577.